Earthquakes as Precursors of Ductile Shear Zones in the Dry and Strong Lower Crust

L. Menegon[1] (iD), **G. Pennacchioni[2]** (iD), **N. Malaspina[3]**, **K. Harris[1,4]**, and **E. Wood[1,5]**

[1]School of Geography, Earth, and Environmental Sciences, Plymouth University, Drake Circus, Plymouth, UK, [2]Department of Geosciences, University of Padova, Padova, Italy, [3]Department of Earth and Environmental Sciences, Università degli Studi di Milano Bicocca, Milano, Italy, [4]Now at Department of Computer Science, University of Warwick, Coventry, UK, [5]Department of Earth, Ocean and Ecological Sciences, University of Liverpool, Liverpool, UK

Abstract The rheology and the conditions for viscous flow of the dry granulite facies lower crust are still poorly understood. Viscous shearing in the dry and strong lower crust commonly localizes in pseudotachylyte veins, but the deformation mechanisms responsible for the weakening and viscous shear localization in pseudotachylytes are yet to be explored. We investigated examples of pristine and mylonitized pseudotachylytes in anorthosites from Nusfjord (Lofoten, Norway). Mutual overprinting relationships indicate that pristine and mylonitized pseudotachylytes are coeval and resulted from the cyclical interplay between brittle and viscous deformation. The stable mineral assemblage in the mylonitized pseudotachylytes consists of plagioclase, amphibole, clinopyroxene, quartz, biotite, ± garnet ± K-feldspar. Amphibole-plagioclase geothermobarometry and thermodynamic modeling indicate that pristine and mylonitized pseudotachylytes formed at 650–750°C and 0.7–0.8 GPa. Thermodynamic modeling indicates that a limited amount of H_2O infiltration (0.20–0.40 wt. %) was necessary to stabilize the mineral assemblage in the mylonite. Diffusion creep is identified as the main deformation mechanisms in the mylonitized pseudotachylytes based on the lack of crystallographic preferred orientation in plagioclase, the high degree of phase mixing, and the synkinematic nucleation of amphiboles in dilatant sites. Extrapolation of flow laws to natural conditions indicates that mylonitized pseudotachylytes are up to 3 orders of magnitude weaker than anorthosites deforming by dislocation creep, thus highlighting the fundamental role of lower crustal earthquakes as agents of weakening in strong granulites.

1. Introduction

Most of crustal seismicity is confined toward the base of the brittle upper crust at temperatures $< 300°C$ (e.g., Chen & Molnar, 1983). Interaction between lower crustal deformation and the earthquake cycle in the overlying seismogenic zone is observed as postseismic afterslip and interseismic creep in the lower crust (Bodin & Horton, 2004; Wright et al., 2013). However, the lower crust is also involved in earthquake nucleation (e.g., Fagereng, 2013; Maggi et al., 2000), and this indicates a mechanically strong lower crust (Jackson et al., 2004; Maggi et al., 2000), at least transiently (Handy & Brun, 2004).

Important volumes of pseudotachylytes (generally interpreted as quenched melts caused by the frictional heat released during seismic slip) in exhumed lower crustal rocks, and formed at lower crustal conditions, have been taken as direct geological evidence for deep fracturing (Austrheim, 2013; Austrheim & Blundy, 1994; Jackson et al., 2004). Examples of deep fracturing is particularly common in dry rocks, and it is generally accepted that a strong, seismogenic lower crust requires anhydrous granulite facies material (Jackson et al., 2004). Anhydrous conditions in granulites inhibit crystal plastic flow and result in high strength (Jackson et al., 2004; Menegon et al., 2011). Furthermore, anhydrous granulites can survive metastably in the course of Wilson cycles, unless they are infiltrated by fluids that trigger metamorphic reactions (Austrheim, 2013). A picture is emerging in which a seismically active lower crust provides an environment for enhanced metamorphic and rheological transitions, due to fluid-rock interaction and associated reaction weakening in the fractured domains (Austrheim, 2013; Austrheim et al., 2017). The observation that viscous shearing in a dry and strong lower crust often localizes in pseudotachylyte veins (Austrheim, 2013; Pennacchioni & Cesare, 1997; Pittarello et al., 2012; Steltenpohl et al., 2006, 2011; White, 1996, 2012) is consistent with this picture. However, the deformation mechanisms responsible for the associated weakening and viscous shear

localization in pseudotachylyte veins are yet to be fully explored. Furthermore, whether lower crustal pseudotachylytes develop by fault-related frictional melting (McKenzie & Brune, 1972), by thermal runaway in ductile shear zones developing extreme localization and accelerated creep rates (John et al., 2009), or by in situ amorphization of crystalline material at high stresses and strain rates (Pec et al., 2012) is still controversial.

Lofoten is one of the rare localities where the interplay between fracturing and viscous flow, and the processes leading to strain localization in dry, granulitic lower crust can be accurately studied, because (1) Lofoten exposes a relatively "intact" lower crust largely consisting of anhydrous granulites (Corfu, 2004), and (2) lower crustal shear zones in Lofoten are commonly associated with large volumes of pseudotachylytes (Steltenpohl et al., 2006, 2011). The study presented here investigates an exceptionally well-preserved network of coeval lower crustal pseudotachylytes and mylonites from Lofoten, and discusses the conditions for pseudotachylytes development and the deformation mechanisms responsible of the ductile shear localization in pseudotachylyte veins.

2. Geological Setting

Lofoten islands in northern Norway consist of a NNE-SSW trending basement horst that is part of the Baltic Shield (Figure 1a). Lofoten represents a tectonic window beneath the Caledonian orogen and is composed of an Archean to Paleoproterozoic metamorphic complex of para and orthogneisses intruded, between 1870 and 1770 Myr, by a large Anorthosite-Mangerite-Charnockite-Granite (AMCG) suite (Corfu, 2004; Griffin et al., 1978). The AMCG suite consists of several plutons of anhydrous composition (Corfu, 2004; Markl et al., 1998) emplaced into the granulitic crust at ambient conditions estimated at 750–800°C, and in the range between 0.4 and 1.0–1.2 GPa (Markl et al., 1998, and references therein). The primary igneous texture and the granulite facies mineral assemblage are generally well preserved.
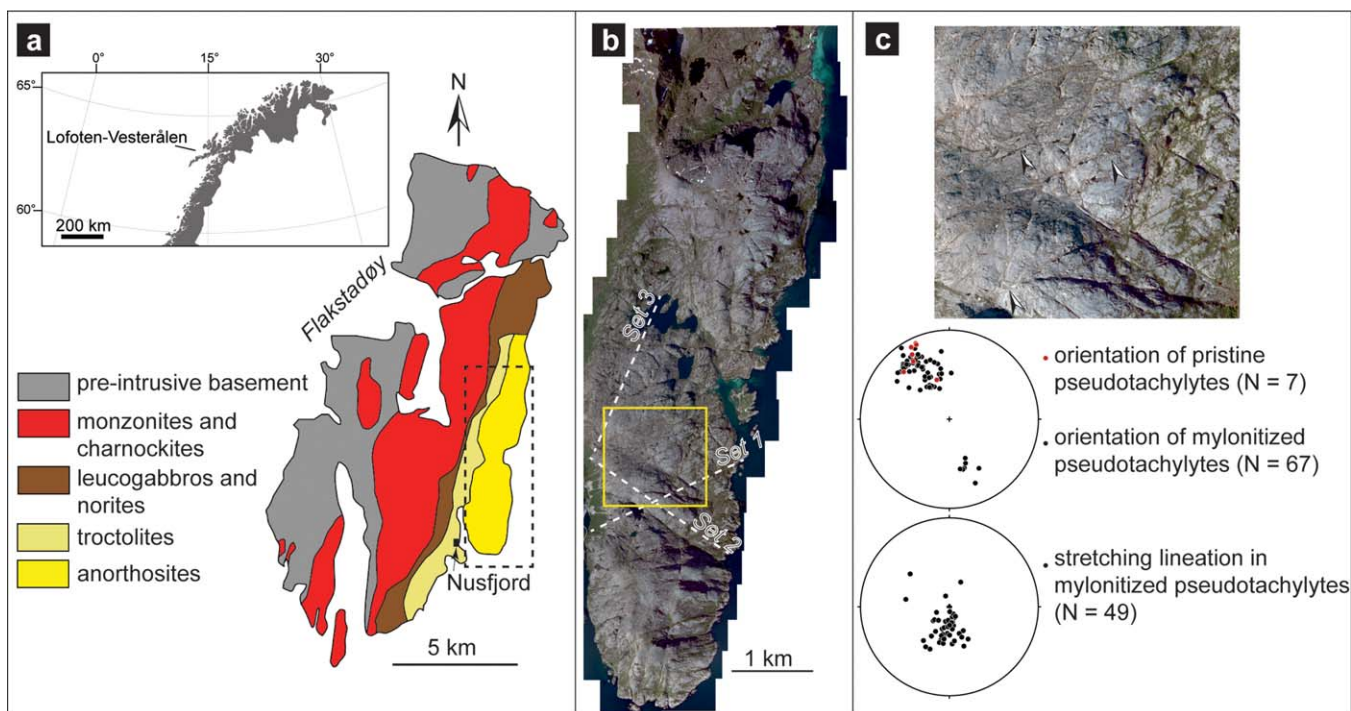
Figure 1. Geological setting. (a) Simplified geological map of Flakstadøy, Lofoten. Modified after Steltenpohl et al. (2006). The dashed rectangle encompasses the area shown in (b). (b) Mosaic of aerial photographs of the Nusfjord ridge. The three main sets of lineaments, defined in the field by ductile shear zones, are marked with white dashed lines. The yellow rectangle encompasses the area shown in (c). (c) Field area investigated in this study. Arrowheads indicate examples of first-order shear zones. Pole figures (lower hemisphere, stereographic projection) showing the orientation of set 1 pristine and mylonitized pseudotachylytes (poles to planes), and of the stretching lineation measured in mylonitized pseudotachylytes. N = number of measurements.

Lofoten largely escaped the Caledonian tectono-metamorphic overprint, as result of water-deficient conditions that inhibited crystal plastic deformation and metamorphic reequilibration of granulites (Leib et al., 2016; Okudaira et al., 2017; Steltenpohl et al., 2004). Despite the lack of a regional postintrusive fabric, eclogite and upper amphibolite facies, localized shear zones are common in Lofoten (Kullerud et al., 2001; Menegon et al., 2013; Steltenpohl et al., 2006, 2011). Fracturing and pseudotachylyte formation have been reported to be key processes for shear zone initiation in Lofoten (Menegon et al., 2013, 2015; Steltenpohl et al., 2006), and available evidence indicates that the pseudotachylytes developed under lower crustal conditions (Moecher & Steltenpohl, 2009).

The Nusfjord eastern ridge in Flakstadøy (Figure 1) exposes one of the largest bodies of anorthosites in Lofoten (Markl et al., 1998). The Nusfjord anorthosites are massive, coarse-grained rocks (1–5 cm average grain size of plagioclase) without any evident solid-state fabric. These rocks host a network of shear zones containing both pseudotachylytes and ultramylonites that are the main subject of this paper.

3. Methods

3.1. Microstructural Observations and Electron Backscatter Diffraction (EBSD) Analysis
Deformation microstructures and petrography were investigated using light and scanning electron microscopy (SEM). Observations were made on polished thin sections cut perpendicular to foliation and parallel to the stretching lineation (mylonites) and perpendicular to the pseudotachylyte vein boundary. SEM analysis was performed at the Plymouth University Electron Microscopy Centre using a JEOL LV6610 SEM and a JEOL 7001 FEG-SEM.

EBSD data were acquired on the JEOL LV6610 SEM equipped with a NordlysNano EBSD detector (Oxford Instruments). Working conditions during acquisition of the EBSD patterns were 20 kV, 70° sample tilt and high vacuum. EBSD patterns were acquired and indexed with the AZtec software on rectangular grids with step size of 0.8 and 2.6 μm, and processed with the Channel 5 software (Oxford Instruments).

3.2. Mineral Chemistry
Major element mineral chemistry was measured with the JEOL 8200 Super Probe electron microprobe analyzer (EMPA) at the Department of Earth Sciences, University of Milan, Italy. Working conditions were 15 kV accelerating voltage, 5 nA current, 1 μm beam diameter, using wavelength dispersive spectrometry (WDS), and natural silicates as standards. All standards were calibrated within 0.5% at one standard deviation and a PhiRhoZ routine was used for matrix correction.

Mineral chemistry of amphibole-plagioclase pairs, used for the of P-T estimates, was measured with the Cameca SX100 microprobe at the School of Earth Sciences, University of Bristol, UK. Working conditions were 20 kV accelerating voltage, 5nA current, 1 μm beam diameter, using wavelength dispersive spectrometry (WDS), and natural silicates as standards. Fe^{3+} of amphiboles and garnets has been calculated from stoichiometry.

3.3. XRF Analysis of Bulk-Rock Chemical Composition
Whole rock chemical analysis of major elements was performed by Wavelength Dispersive X-Ray Fluorescence (WD-XRF) analysis with a Philips PW2400 equipped with a rhodium tube at the Department of Geosciences, University of Padova, Italy. Powder samples were mixed and diluted at 1:10 with $Li_2B_4O_7$ and $LiBO_2$ flux and melted into glass beads. Loss on Ignition (LOI) was determined from weight lost after ignition at 860°C for 20 min and at 980°C for 2 h. FeO was determined with permanganometry using a rhodium tube.

3.4. Thermodynamic Modeling
H_2O-saturated P-T and T-H_2O isochemical sections were calculated with Perple_X software (Connolly, 2005), in the system SiO_2-Al_2O_3-MgO-CaO-Na_2O-K_2O-TiO_2-FeO-(Fe_2O_3), using the bulk composition of the mylonitized pseudotachylyte sample N13-10D and of the host anorthosite sample N13-10B (Table 1). We used the thermodynamic database and equation of state for H_2O of Holland and Powell (1998, upgrade 2002) and no phase was excluded from the calculation. We

Table 1
Representative Whole Rock XRF Analysis of Anorthosites, of Pristine, and of Mylonitized Pseudotachylytes

Lithology	Anorthosite host rock	Pristine pseudotachylyte	Mylonitized pseudotachylyte
Sample	N13-10B	N22	N13-10D
Sample location	0432042 E 7549520 N	0432009 E 7550172 N	0432042 E 7549520 N
SiO_2	53.83	51.37	53.54
TiO_2	0.14	0.32	0.30
Al_2O_3	27.22	25.67	25.11
Fe_2O_{3tot}	1.37	3.98	3.80
MnO	0.02	0.04	0.04
MgO	0.41	1.87	1.86
CaO	10.75	10.85	9.89
Na_2O	4.75	4.25	4.24
K_2O	0.61	0.76	0.92
P_2O_5	0.04	0.04	0.04
Tot	99.14	99.15	99.74
FeO	*n.d.*	*n.d.*	*3.32*
L.O.I.	*0.32*	*0.30*	*0.32*

Note. GPS coordinates are relative to WGS84, zone 33 W.

used the solution models of Holland and Powell (1998, 2003) for olivine, orthopyroxene, clinopyroxene, garnet, spinel, phengite, and feldspar, of Tajcmanova et al. (2009) for Ti-biotite, and of Dale et al. (2005) for calcic amphibole.

3.5. SIMS Analysis

Intracrystalline hydrogen content in plagioclase was measured on polished thin sections using the Cameca ims-4f Secondary Ion Mass Spectrometry (SIMS) at the NERC Ion Microprobe Facility in Edinburgh, UK. Prior to analysis, the sample was placed in an oven at 105°C for 30 min to remove surface humidity. The sample was then coated with a gold film (<0.02 μm) and kept in the SIMS chamber under high vacuum (5×10^{-9} Torr) for >48 h. Analysis was performed with a 5 nA primary beam of $^{16}O^-$ ions accelerated to 14.5 kV. To avoid surface contamination, few nanometers of surface material were removed by sputtering the spot for 4 min while rastering the beam (25 μm grid) before each measurement. Measurements were acquired using a beam spot size of 20 μm (± 5 μm). Each analysis consisted of 20 cycles of the isotopes ^{1}H, ^{23}Na, ^{30}Si, ^{39}K, and ^{49}Ti. For hydrogen only the last 15 cycles were averaged as ^{1}H signals stabilized only after the first cycles. Previously determined SiO_2 concentration was used as internal standard. Probing locations were identified beforehand and attention was paid to avoid cracks, grain-boundaries, and alterations, which could contain free water. Basaltic glass standard St81A9 (Lesne et al., 2011) was used to calibrate the water content in plagioclase. Anhydrous olivine standard (Kilbourne Hole) was used to correct for background ^{1}H signals (estimated at 12 wt. ppm H_2O).

4. Field Observations

The eastern ridge of Nusfjord peninsula is dominated by coarse-grained anorthosites with minor troctolites and gabbros. Satellite images show a network of three main sets of lineaments trending ENE-WSW to NE-SW (*Set 1*), NW-SE (*Set 2*), and NNE-SSW (*Set 3*) (Figures 1b and 1c). In the field, the lineaments correspond to major (of as much as a few meters wide), steeply dipping mylonitic shear zones associated with subparallel second-order (cm–dm thick) discrete shear zones in between (Figure 2). All three sets contain associations of pseudotachylytes and mylonites. The study presented here focuses on the *Set 1* shear zones, because it contains the largest volumes of pseudotachylytes in the area.

Set 1 shear zones dip steeply mostly towards the SE and contain a moderately to steeply plunging stretching lineation (Figure 1c). The shear zones show normal-oblique kinematics, with a top-to-S component. The simplest type of second-order shear zone consists of a thin sharply bounded, homogeneously fine-grained (Figures 2a–2c), dark green sheared layer. This layer is typically surrounded by a < 10 cm wide bleached halo (contrasting in color with the dark host anorthosite), which was partly involved in shearing (Figures 2a–2c). The bleached halo results from a pervasive network of white-colored layers forming transgranular microfractures or exploiting the cleavage of the coarse anorthosite plagioclase (Figure 2c).

The dark layers are homogeneously fine-grained, regardless of the accommodated strain (Figure 2d), indicating that the fine grain size did not result from progressive grain size refinement, but was a pristine feature of the shear zone precursor. These layers are identified as sheared pseudotachylyte fault veins as indicated by the local preservation of pseudotachylyte breccia pockets (Figure 2e) and injection veins (Figures 2f and 2g), and by the local occurrence of undeformed pseudotachylytes trending parallel to the shear zones (Figure 2h).

Thick shear zones have commonly a domainal foliation defined by elongated, alternating domains of whitish and dark-green color (Figures 3a and 3b). These latter domains are fine-grained and similar to the deformed pseudotachylytes of the second-order shear zones; locally they are discordant to the main foliation (Figure3a). There is no compositional heterogeneity in the pristine anorthosite to explain the origin of such compositional banding of mylonitic rocks. The dark domains tend to anastomose around the white domains that represent stretched portions of the bleached/damaged host anorthosite. With increasing strain both types of domains tend to form a more regular, planar layering and macroscopic plagioclase porphyroclasts disappear. Large, low strain domains associated with some major shear zones locally show thick (20–50 cm) pseudotachylyte breccias with cm-sized lithic clasts of bleached anorthosite and clast-free layers of pseudotachylyte (Figure 3c), parallel to the shear zone boundary. The origin of the sheared dark domains
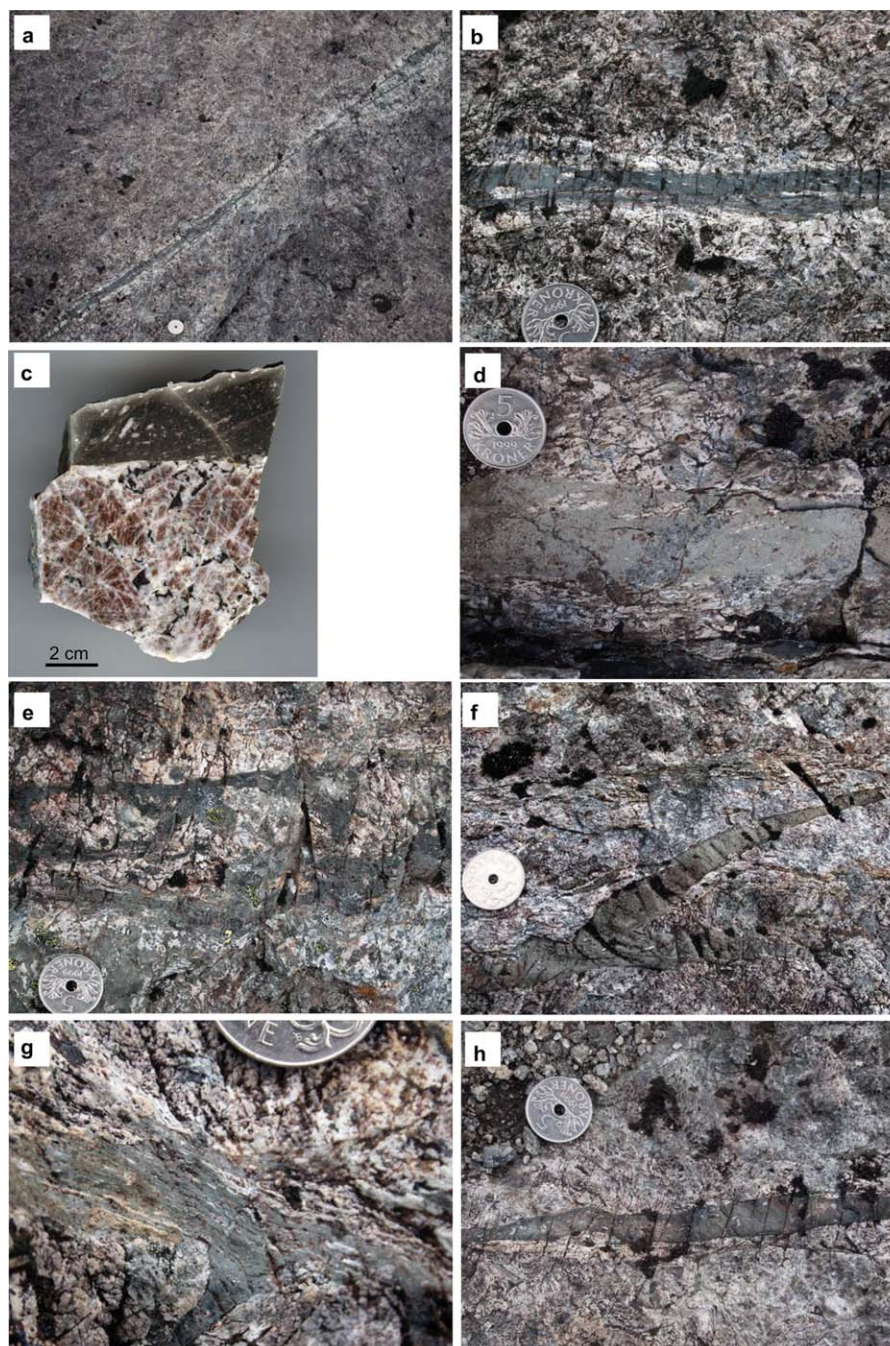
Figure 2. Field structures of second-order shear zones and of pseudotachylyte. All GPS coordinates are relative to WGS84, zone 33W. (a) Thin (<2 cm) ductile shear zone surrounded by a bleached halo within the darker coarse grained anorthosite. GPS coordinates: 0431864 East, 7549944 North. (b) Detail of the shear zone in Figure 2a showing the fine grained, dark green, sharply bounded mylonitic core surrounded by a partially sheared bleached halo. (c) Polished sample of a weakly deformed dark-green shear zone in sharp contact with the host anorthosite. The coarse (cm-sized) purple-colored magmatic crystals of anorthosite show bleaching along a pervasive network of microfractures. GPS coordinates: 0431685 East, 7549992 North. (d) Relatively weakly deformed pseudotachylyte with lithic clasts of the bleached anorthosite deformed to elongated domains stretched oblique to the pseudotachylyte (shear zone) boundary. Same locality as Figure 2c. (e) Pseudotachylyte breccia with bleached lithic clasts and host rock; GPS coordinates: 0431808 East, 7550038 North. (f) Pristine pseudotachylyte injection vein protruding from a fault vein. Same locality as Figure 2e. (g) Sheared pseudotachylyte fault vein preserving an undeformed injection vein in the host anorthosite. GPS coordinates: 0432073 East, 7550013 North. (h) Pristine pseudotachylyte preserving chilled margins and small equant clasts of bleached plagioclase. Same locality as Figure 2e. Coin for scale (2.5 cm in diameter) in all the field photographs.
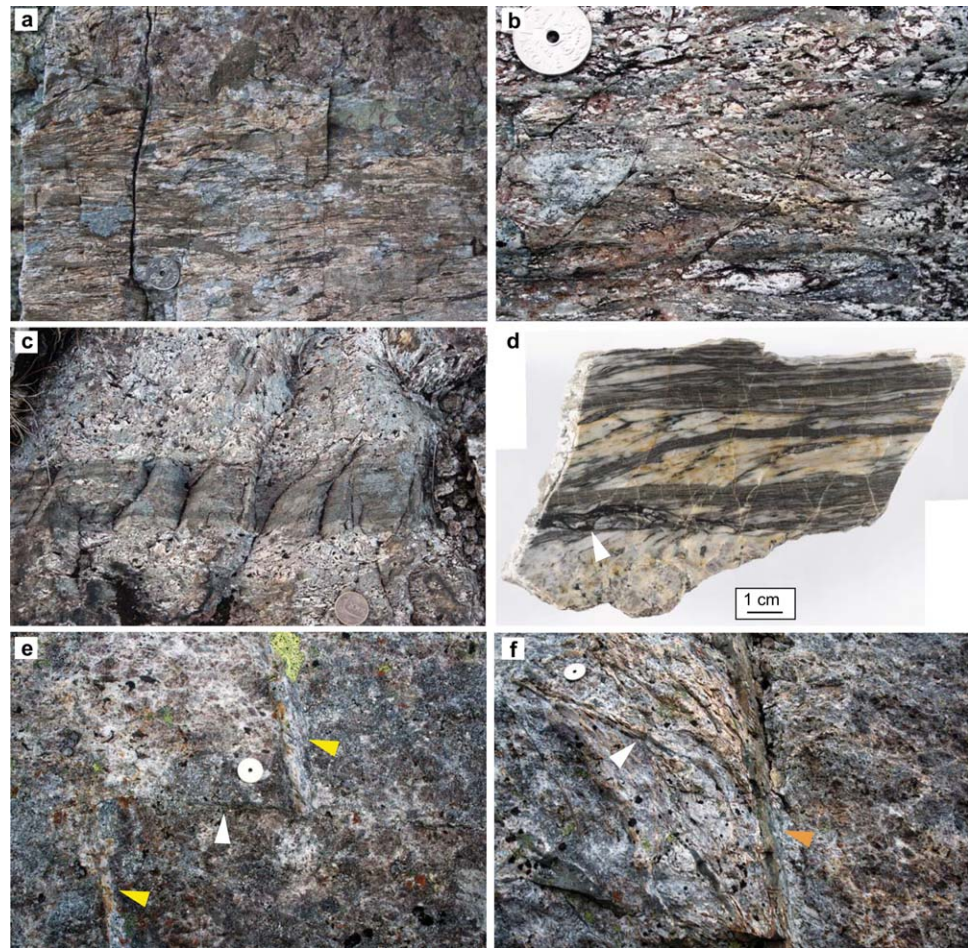
Figure 3. Field structures of major shear zones and associated pseudotachylytes. All GPS coordinates are relative to WGS84, zone 33W. (a) Mylonitic foliation with alternating thin bands of green and whitish color. Note that some green layers are still locally discordant to the foliation and that pristine pseudotachylyte injection veins are present in the host anorthosite. GPS coordinates: 0432042 East, 7549520 North. (b) Large domain of weakly mylonitized pseudotachylyte breccia with variably flattened and stretched lithic clasts of the bleached anorthosite. GPS coordinates: 0432009 East, 7550172 North. (c) Similar as Figure 3b but also showing a thick central pseudotachylyte layer localizing the deformation. Same locality as Figure 3b. (d) Polished sample of a domainal foliation delineated by green and whitish layers, derived from pseudotachylyte and bleached anorthosite. In the lower part of the sample, a pseudotachylyte exploited the shear zone boundary and the mylonitic foliation was brecciated within a side wall ripout. Same locality as Figure 3a. (e and f) A pristine pseudotachylyte (indicated with a white arrowhead) sharply displaces a whitish localized shear zone (yellow arrowheads) (e) and is in turn dragged into the mylonitic foliation along a dm-thick shear zone with domainal green-whitish layering (orange arrowhead) (f). GPS coordinates: 0432232 East, 7549970 North. Coin for scale (2.5 cm in diameter) in all the field photographs.

from pseudotachylytes is indicated by the common occurrence of undeformed pseudotachylyte injection veins in the anorthosite wall rock of shear zones.

In some cases, the pseudotachylyte veins crosscut the mylonitic foliation. In Figure 3d, the foliation of a shear zone, that includes sheared pseudotachylytes, is involved in a breccia cemented by a pseudotachylyte that exploited the shear zone boundary. Figure 3e shows a pseudotachylyte-bearing fault sharply displacing a localized ductile shear zone and being in turn dragged into a ductile shear zone that exploits older pseudotachylyte veins (Figure 3f).

5. Microstructure

5.1. Anorthosite Host Rock

Anorthosite consists of large (as much as 20 cm in size) plagioclase crystals and subordinate (<10%) clinopyroxene, orthopyroxene, and olivine (Figure 4a). Clinopyroxene is the most common mafic phase. Hydrous
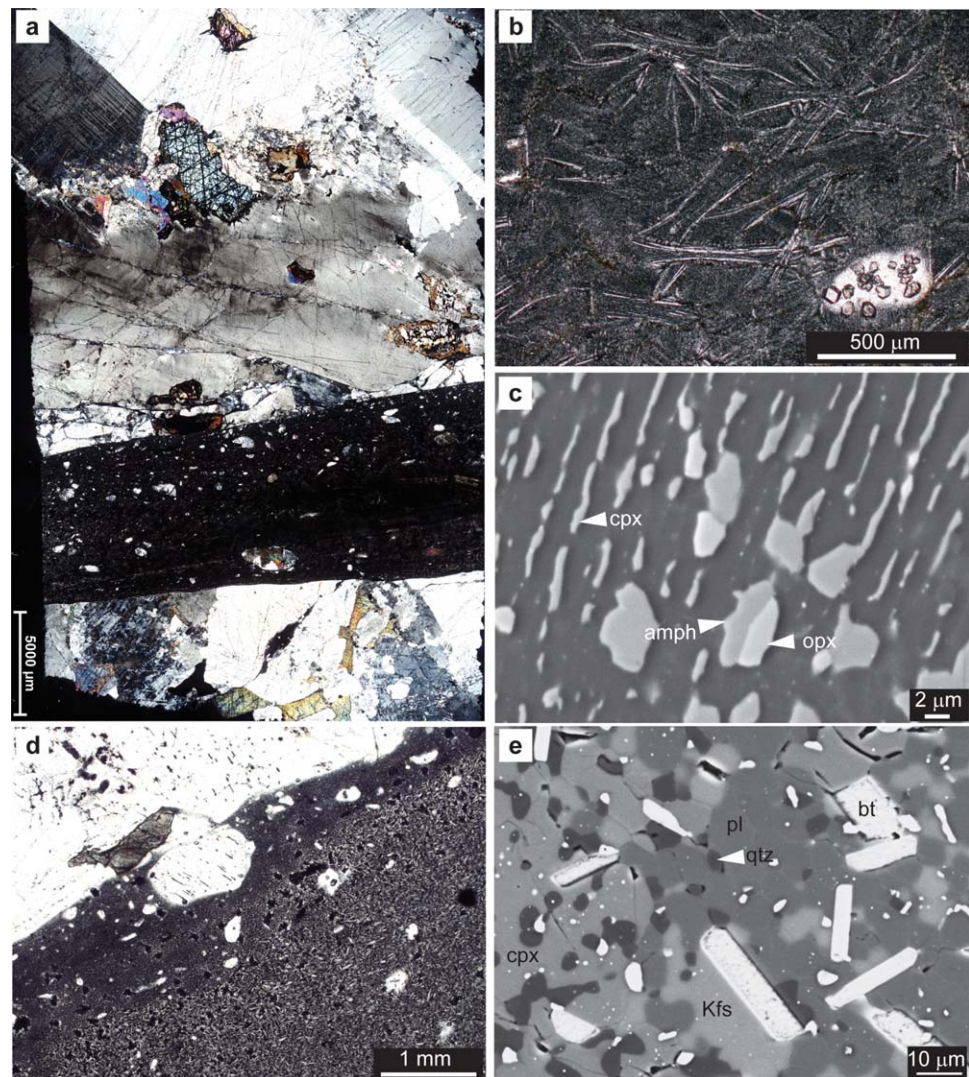
Figure 4. Representative microstructures of pristine pseudotachylytes. Mineral abbreviations: amph = amphibole, bt = biotite, cpx = clinopyroxene, Kfs = K-feldspar, pl = plagioclase, qtz = quartz. (a) Thin section of a pristine pseudotachylyte vein and of the anorthosite host rock. Crossed polarizers. (b) Plagioclase survivor clast and microlitic microstructure. Note the cluster of garnet grains overgrowing the plagioclase survivor clast. Parallel polarizers. (c) SEM backscatter electron image of microlites of clinopyroxene, orthopyroxene, amphibole and plagioclase (dark grey phase). (d) Example of chilled margin of a pseudotachylyte vein. Parallel polarizers. (e) SEM backscatter electron image of the fine-grained phase mixture found in the recrystallized pseudotachylytes.

phases are very rare (<1%) and consist of local biotite rims around orthopyroxene and of discontinuous amphibole coronas around clinopyroxene. Corundum locally occurs as idiomorphic single crystals or as aggregates included in mm-sized magnetite. A detailed description of the Nusfjord anorthosites is reported in Markl et al. (1998).

5.2. Pseudotachylyte and Associate Damage Zone

Pseudotachylytes locally preserve the pristine microstructure that includes microlites of plagioclase, clinopyroxene, amphibole, and orthopyroxene (Figures 4a–4c), flow structures, and chilled margins (Figure 4d). Pristine pseudotachylytes consist of single-generation individual veins with no evidence of multiple veins along the same fault.

The pseudotachylyte matrix is microcrystalline and dominantly consists of very fine-grained (<5 μm) plagioclase. Plagioclase, and rarer clinopyroxene and orthopyroxene, occur as clasts in the pseudotachylyte matrix together with lithic clasts. The shape of clasts ranges from angular to smoother

shapes showing resorption structures. In the damage zone flanking pseudotachylyte, plagioclase and clinopyroxene show undulatory extinction, bent twins and bent lamellae (in pyroxenes). The grains show fractures filled with new small polygonal grains (20–30 μm in size) forming bands up to 100 μm wide (Figure 4a). In clinopyroxene the intracrystalline bands of new grains locally contain minor amounts of amphibole.

Some pseudotachylytes have completely lost the pristine microlitic microstructure and have recrystallized into a fine-grained (average grain size ~10 μm) mixture of plagioclase, amphibole, clinopyroxene, biotite, quartz ± K-feldspar ± orthopyroxene ± ilmenite (Figure 4e). Since these pseudotachylytes do not show a mylonitic overprint, we refer to them as to *recrystallized pseudotachylytes*.
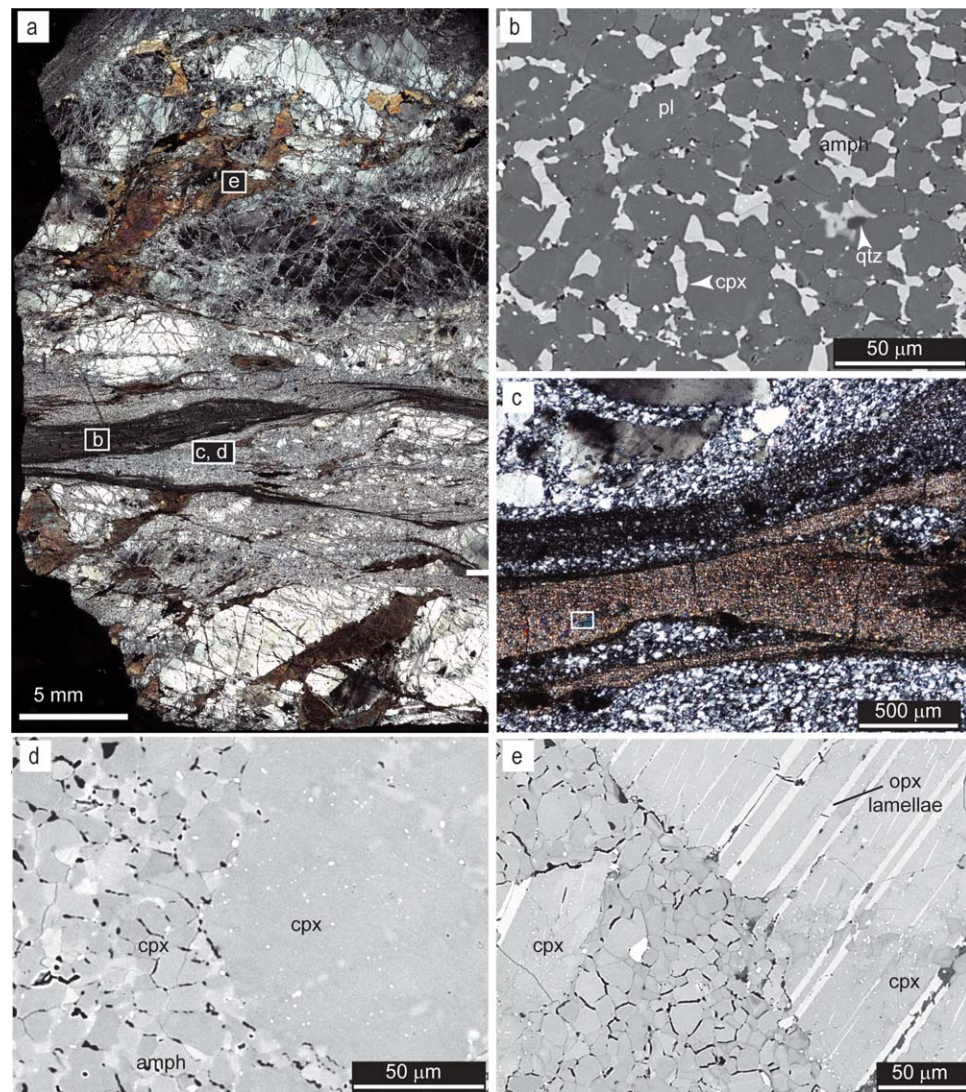

Figure 5. Representative microstructures of ductile shear zones. Mineral abbreviations like in Figure 4. (a) Thin section of a ductile shear zone consisting of mylonitized pseudotachylytes (transposed and sheared dark veins) and of variably fractured and recrystallized anorthosite. Black rectangles show the microstructural position of Figures 5b–5e. Crossed polarizers. (b) SEM backscatter electron image of the fine-grained mylonitized pseudotachylyte vein shown in Figure 5a. (c) Bands of recrystallized plagioclase (with relict fragments of magmatic grains) alternating with clinopyroxene-derived aggregate (brown band) along the shear zone foliation. The clinopyorexene-derived aggregate consists of clinopyroxene porphyroclasts embedded in a fine-grained matrix of clinopyroxene, amphibole and quartz. Light microscope image, crossed polarizers. The white rectangle shows the approximate position of Figure 5d. (d) SEM backscatter electron image of a detail of the site shown in Figure 5c. (e). Fractured clinopyroxene in the damage zone flanking the shear zone. The intracrystalline fracture is filled with small grains of clinopyroxene and amphibole.

Garnet is common in pristine and recrystallized pseudotachylytes as well as in the wall rock anorthosite. In pristine pseudotachylytes, garnet occurs as small (50–100 μm) euhedral grains arranged as: (i) overgrowths on plagioclase clasts (Figure 4b); (ii) framboidal rims around opaque grains; (iii) trails along thin healed microcracks confined within the pseudotachylyte vein; and (iv) trails along the pseudotachylyte boundary.

5.3. Ductile Shear Zones

Mylonitized pseudotachylytes consist of a fine-grained (average grain size: 5–30 μm) mixture of plagioclase, amphibole, and clinopyroxene, with less abundant garnet, biotite, quartz, K-feldspar, and ilmenite (Figure 5b). Amphibole is typically found as isolated grains and small clusters (<50 μm in length) at triple junctions
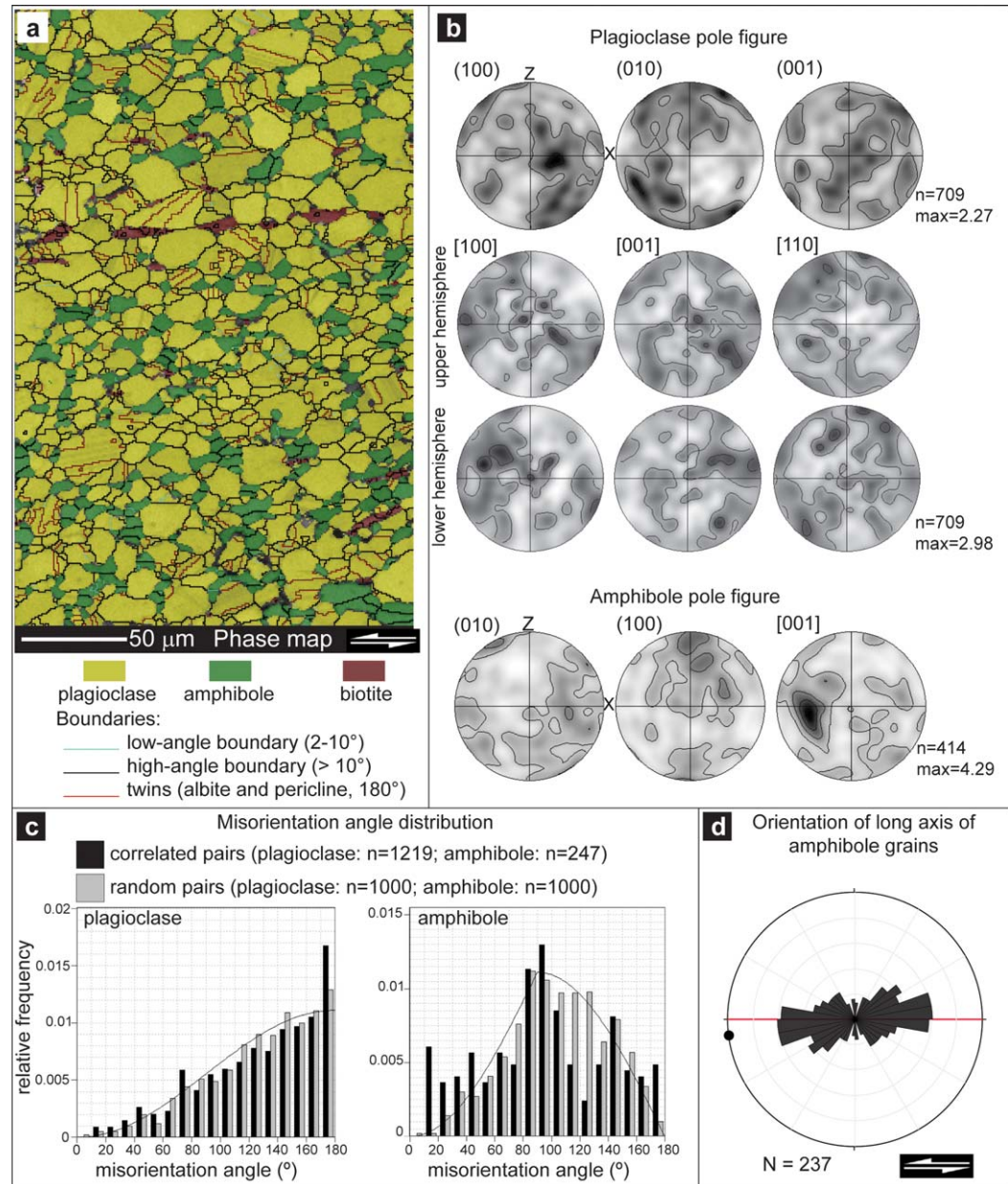
Figure 6. EBSD analysis of a mylonitized pseudotachylyte vein. (a) Phase map of a fine-grained mylonitized pseudotachy-lyte. (b) Contoured pole figures (half width 15°, data clustering 5°) of plagioclase and amphibole from the site shown in Figure 6a, plotted as one point per grain (n = number of grains). Black color marks maxima, also given as multiples of the uniform distribution. (c) Histograms of misorientation axis distribution of plagioclase and amphibole form the site shown in Figure 6a. The theoretical curves for a random orientation are also shown. (d) Rose diagram showing the orientation of the long axis of amphibole grains included in Figure 6a. The red line is parallel to the trace of the shear zone boundary.

between plagioclase grains (Figure 5b), as well as along C' shear bands. The amount of amphibole in the phase mixture, estimated with image analysis on SEM backscatter electron images, is in the range of 5–10 vol. %. Garnet is present as isolated grains (typically $< 20\ \mu m$ in size) dispersed in the phase mixture, and as polycrystalline clusters where individual grains are up to $200\ \mu m$ in size (supporting information Figure S1). Most of the garnets contain inclusions of plagioclase, clinopyroxene, and amphibole. Isolated grains of garnet are typically inclusion-free.

Mylonitic pseudotachylytes wrap around lenses deriving from the grain-size reduction of original plagioclase and clinopyroxene of the anorthosites. In these lenses, plagioclase is variably fractured and recrystallized to fine-grained (average grain size of $25\ \mu m$) monomineralic aggregates elongated parallel to the shear zone foliation. The relict porphyroclasts show undulatory extinction and bent twins (Figures 5a and 5c). Clinopyroxene porphyroclasts are partially to completely replaced by fine-grained ($<30\ \mu m$) clinopyroxene, amphibole, and quartz neoblasts along intracrystalline bands and along the boundaries with plagioclase (Figure 5d). The clinopyroxene-derived aggregates are also stretched parallel to the mylonitic foliation (Figure 5c).

Plagioclase and clinopyroxene in the damage zone flanking the ductile shear zones are pervasively fractured and show undulatory extinction. Fractures are filled with new small polygonal grains of plagioclase (within plagioclase) and clinopyroxene + amphibole $\pm$ quartz (within clinopyroxene). The new grains are 5–30 μm in size and form up to $200\ \mu m$ wide intracrystalline bands (Figure 5e). These microstructures are identical to those of the damage zone flanking pristine pseudotachylyte veins.

6. EBSD Analysis

The crystallographic preferred orientation (CPO) of plagioclase determined by EBSD in the polyphase matrix of the mylonitic pseudotachylyte (Figure 6a) does not show an obvious alignment of lattice planes and axes
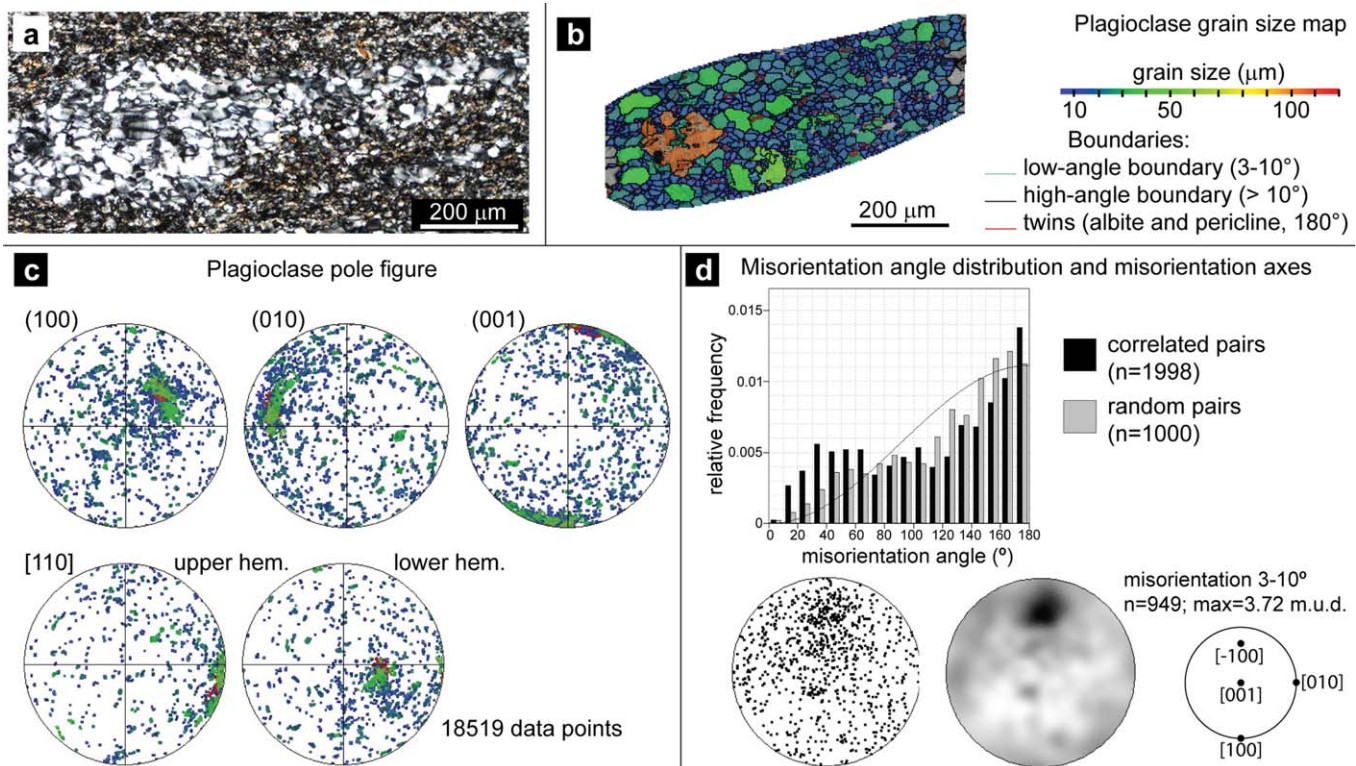
Figure 7. EBSD analysis of a recrystallized plagioclase aggregate embedded in a mylonitized pseudotachylyte vein. (a) Microstructure of the analyzed aggregate. Crossed polarizers. (b) Grain size map of the plagioclase aggregate shown in Figure 7a. The large grain color-coded orange in interpreted as a relict fragment of the primary plagioclase grain. (c) Plagioclase pole figure of the grains included in Figure 7b, and color coded like the grain size map shown in Figure 7b. (d) Misorientation angle distribution histogram of plagioclase and misorientation axis for misorientations of 3–10° plotted in crystal coordinates, both as point data and as contoured plot. The theoretical curve for a random distribution and the crystal coordinate system of plagioclase are also shown.

with the foliation and with the stretching lineation, respectively (Figure 6b). On the contrary, amphibole has a CPO of the (100) planes distributed along a discontinuous girdle subparallel to the YZ plane of the finite strain ellipsoid, with a maximum near the pole to the foliation (Figure 6b). The [001] axis forms a maximum on the foliation plane at a low angle to the stretching lineation.

The misorientation axis distribution (MAD) of random pairs of both plagioclase and amphibole is remarkably close to the theoretical curve for a random distribution (Figure 6c). Correlated pairs of both plagioclase and amphibole show that misorientations $< 50°$ occur with a higher frequency than for a random distribution (Figure 6c).

The long axes of amphibole grains are preferentially oriented at an angle of 5–20° measured counterclockwise from the trace of the ultramylonite foliation (Figure 6d). For the sinistral sense of shear of the ultramylonite in Figure 7a, the preferred orientation of the long axes of amphibole corresponds to a C′-type shear band orientation.

Recrystallized plagioclase in an elongated monomineralic aggregate embedded in mylonitized pseudotachylytes (Figure 7a) shows a grain size range from 4 μm to about 120 μm (Figure 7b). Grains larger than 30 μm are preferentially oriented with the (001) planes subparallel to the foliation and with the [110] direction subparallel to the stretching lineation. Grains smaller than 30 μm show a remarkable dispersion of the crystallographic planes and axes, but many small grains overlap in orientation with the larger grains (Figure 7c). Misorientations $< 70°$ occur with a higher frequency than for a theoretical random distribution for both correlated and uncorrelated pairs (Figure 7d). The misorientation axis for low misorientations (3–10°) is preferentially parallel to the [–100] axis (Figure 7d).

7. Mineral Chemistry and P-T-H_2O Conditions of Deformation

The major element compositions of representative minerals in pristine, recrystallized, and mylonitized pseudotachylytes are reported in supporting information Tables S1–S3. Plagioclase of the host rock has ~77 mol. % of anorthite component (bytownite). Plagioclase microlites and recrystallized plagioclase (both in recrystallized and in mylonitized pseudotachylytes) have lower anorthite contents, mostly in the range between 46 and 52 mol. % (andesine), but with a few recrystallized grains containing up to 58 mol. % of anorthite (supporting information Table S1).

Clinopyroxene is diopside, with similar Al contents of 0.15–0.20 atoms per formula unit (a.p.f.u.) in both the host rock and in the recrystallized grains in the mylonite (supporting information Table S2). X_{Mg} values (Mg/(Mg + Fe^{2+})) range from 0.76 to 0.84, with the highest values found in clinopyroxene inclusions in garnet (supporting information Table S2). Orthopyroxenes occur in the host rock, as survivor clasts and as microlites in the pseudotachylytes, and as porphyroclasts in the mylonites. They have similar compositions with X_{Mg} of ~0.57–0.68 and Al contents from 0.10 to 0.14 a.p.f.u., and up to 0.20 a.p.f.u. in the microlites (supporting information Table S2).

Amphiboles are pargasites and have Ca ~1.90, (Na + K)$_A$ from 0.71 to 0.85 and Si ranging from 5.98 to 6.35 a.p.f.u. (supporting information Table S3). The values of X_{Mg} range from 0.55 to 0.63, up to 0.68 for those included in garnet in the mylonites. Amphiboles do not show
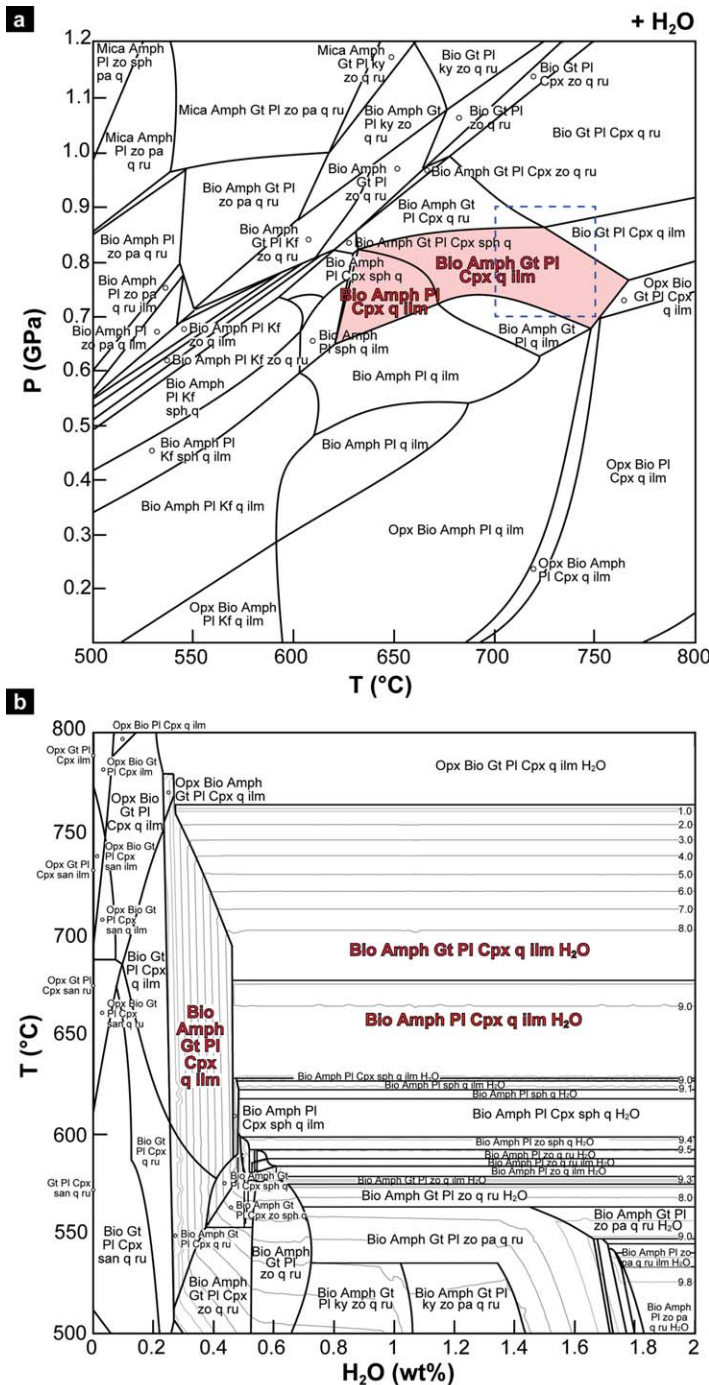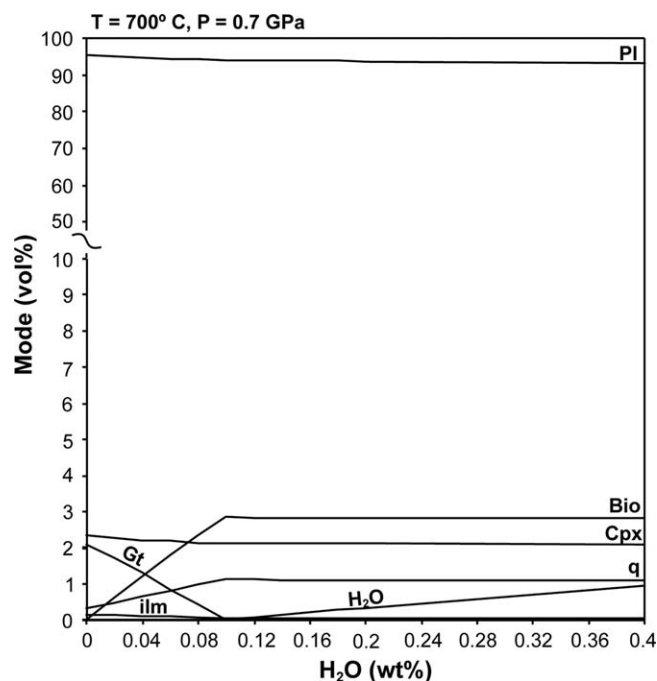
Figure 8. (continued)

Figure 9. Modal phase abundances (vol. %) of the isochemical section calculated at 0.7 GPa and 700°C for the pristine anorthosite, calculated in the system SiO_2 (53.83) – Al_2O_3 (27.22) – MgO (0.41) – CaO (10.75) – Na_2O (4.75) – K_2O (0.61) – TiO_2 (0.14) – FeOtot (1.23). Mineral and solid solution abbreviations are the same as in Figure 8.

any variation of $(Na + K)_A$ and $Al^{(VI)}$ indicative of edenite substitution. Almost homogeneous composition of amphiboles in the various microstructural sites of pristine, recrystallized and mylonitized pseudotachylytes suggests similar equilibrium conditions during the formation, recrystallization, and shearing of pseudotachylytes.

Supporting information Table S3 also shows the compositions of garnets overgrowing plagioclase survivor clasts in pseudotachylytes, in coronas around corundum in the host rock, and in the mylonitized pseudotachylytes. All garnets have the same almandine content (~50 mol. %), except those around corundum (59 mol. %). They instead record variable grossular and pyrope contents with values ranging from 28 to 39 mol. % of grossular, corresponding to a variation from 24 to 11 mol. % of pyrope (supporting information Table S3).

Supporting information Tables S1 and S3 also report representative compositions of plagioclase and amphibole pairs used for conventional geothermobarometry calculations. Temperature was estimated with the thermometer of Holland and Blundy (1994), which considers the exchange reaction edenite + albite = richterite + anorthite and was calibrated in the P, T range of 0.1–1.5 GPa and 400–1000°C. Pressure was estimated with the barometer of Anderson and Smith (1995), which is based on the increase of Al content in hornblende with increasing P and was calibrated in the T range between 675 and 760°C. The resulting P, T conditions of sin-kinematic recrystallization in the mylonitized pseudotachylytes are estimated at 700–750°C, 0.7–0.9 GPa.

These results are in agreement with the P-T stability field modeled in Figure 8a for H_2O-saturated conditions, which were chosen because we interpret the synkinematic nucleation of amphibole at triple junctions as the evidence of the presence of H_2O at grain boundaries. The mineral assemblage consisting of biotite – amphibole – plagioclase – clinopyroxene – quartz – ilmenite found along the recrystallized and mylonitized pseudotachylytes (Figures 4e, and 5b) is stable in the red P-T area of Figure 8a, at around 650°C and 0.7 GPa. Syn to postkinematic garnet extends the stability field up to 750°C and 0.85 GPa. These maximum temperatures correspond to the stability limit of amphibole for the studied composition. Below 750°C, the stability of amphibole is also governed by the amount of water assisting the deformation, as portrayed in the T-X(H_2O wt. %) section of Figure 8b, calculated at 0.7 GPa. At least 0.25 wt. % of H_2O is required to crystallize amphibole and 0.5 wt. % to saturate the system in the temperature range from 575 to 750°C. For higher H_2O contents, the modal amount of amphibole is only dependent on the equilibration temperature, as shown by the grey lines that indicate the locus of points of equal amount (vol. %) of amphibole for the various modeled mineral assemblages.

To evaluate if fluid infiltration was required in order to stabilize the mineral assemblage of the mylonitzed pseudotachylytes, we modeled the variation of modal abundances of mineral phases in the pristine anorthosites as a function of the H_2O content. The calculations have been performed at the estimated P, T conditions of deformation (700°C and 0.7 GPa) and the results are shown in Figure 9. The diagram shows

Figure 8. (a) Isochemical P–T section for mylonitized pseudotachylyte calculated in the system SiO_2 (53.03) – Al_2O_3 (24.84) – MgO (1.87) – CaO (9.96) – Na_2O (4.24) – K_2O (0.89) – TiO_2 (0.31) – FeO (3.32) – Fe_2O_3 (0.11). Values in brackets are oxide wt. %. The red area shows the hypothetical stability field of the mylonite paragenesis, as evidenced by microstructural and mineral chemistry analyses. Abbreviations for solid solution models: Amph – amphiboles; Bio – biotite; Cpx – clinopyroxene; Gt – garnet; Kfs – alkali feldspar; Mica – phengite; Pl – ternary feldspar. Abbreviations for phases: zo, zoisite; sph, titanite (sphene); q, quartz; pa, paragonite; ky, kyanite; ru, rutile; ilm, ilmenite. The dashed blue rectangle shows the P, T conditions estimated with amphibole-plagioclase geothermobarometry. (b) Isochemical T-H_2O section (same composition) calculated at 0.7 GPa, showing the stable paragenesis from dry conditions up to 2 wt. % of water. In the temperature range of interest (600–750°C), the system becomes H_2O saturated (i.e., free water) when the H_2O of the bulk composition is higher than 0.3–0.5 wt. % (depending on the temperature). The grey lines and the corresponding numbers on the right-hand side of the plot indicate the amount of amphibole (vol. %) occurring in the mineral assemblage.
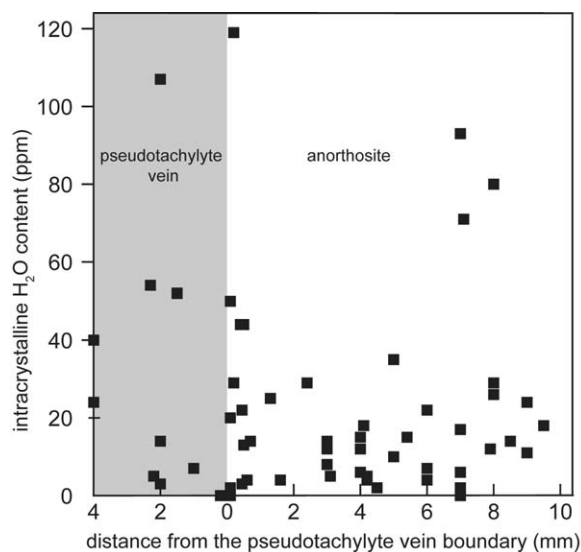
Figure 10. Results of the ion microprobe measurements of intracrystalline water content in plagioclase. The area shaded in grey corresponds to the interior of a pristine pseudotachylyte vein.

that < 1 vol. % of biotite requires approximately 0.04 wt. % of H_2O, and that such a low amount of H_2O would not result in the presence of free intergranular H_2O in the anorthosite protolith at the estimated P, T conditions of deformation. Thus, the amount of fluid present in the anorthosite is about 6–10 times less than that required to stabilize the mineral assemblage of the mylonitized pseudotachylytes.

8. Intracrystalline Water Content in Plagioclase

Brittle fracturing can introduce fluids into grain interiors even at high P-T conditions and this typically favors hydrolytic weakening (e.g., Stünitz et al., 2017). The measurement of the intracrystalline water content in plagioclase was carried out to test if fracturing and pseudotachylyte formation was accompanied by fluid infiltration in the interior of the grains. We measured the intracrystalline H content in plagioclase grains along 1.5 cm long transects from the undeformed anorthosite to the pristine pseudotachylyte, where the measurements were restricted to survivor clasts.

Most of the measurements indicate intracrystalline water contents < 40 ppm both in the anorthosites and in survivor clasts in the pseudotachylyte (Figure 10). There is no progressive increase of water concentration in plagioclase towards the pseudotachylyte vein, and many clasts inside the veins and at the pseudotachylyte vein boundary have water concentration < 20 ppm. There are few grains with intracrystalline water content > 70 ppm both in the host rock and in the pseudotachylyte. SEM inspection of the probe pits indicates that these higher water concentrations occur in close proximity to lamellae of K-feldspar, presumably resulting from exsolution of original ternary feldspars (supporting information Figure S2).

9. Discussion

9.1. Cyclic Interplay Between Brittle and Viscous Deformation at Lower Crustal Conditions

Field observations in Nusfjord indicate that ductile shear zones exploited a set of pseudotachylyte-bearing faults. This is consistent with the general observation that nucleation of ductile shear zones requires the presence of a planar compositional or structural precursor (e.g., Pennacchioni & Mancktelow, 2007; Pennacchioni & Zucchi, 2013). In Nusfjord, pseudotachylytes provided both the structural anisotropy of long, subparallel fault planes and the compositional precursor of weak, fine-grained pseudotachylyte fault veins decorating the slip surfaces. The alternation of thinner and thicker shear zones apparently reflects the original hierarchical organization of the precursor pseudotachylyte-bearing faults (Di Toro & Pennacchioni, 2005; Pennacchioni, 2005). Thin shear zones derive from single mm-cm thick pseudotachylyte fault veins that only locally include pockets of pseudotachylyte breccias. Major shear zones overprinted complex bands of more pervasive pseudotachylyte veining and brecciation.

The mutual overprinting relationships between pristine and mylonitized pseudotachylytes (Figures 3d and 3f) are interpreted to result from the cyclic interplay between brittle and viscous deformation. Thus, the P-T conditions of deformation estimated for the mylonitized pseudotachylytes are considered representative also of the conditions of formation of pseudotachylytes. This is supported by the similarity in microstructure of the damage zone flanking both pristine and mylonitized pseudotachylytes showing neoblasts of clinopyroxene and amphibole, and the lack of low-grade minerals (Figures 4a and 5e).

The P-T conditions of deformation are constrained at 650–750°C and 0.7–0.8 GPa (depending on the stability of garnet), using both amphibole-plagioclase conventional geothermobarometry and thermodynamic forward modeling. Assuming an average crustal rock density of 2,700–3,000 kg/m^3, these conditions correspond to a depth range of 24–30 km and indicate a lower crustal setting for the brittle-viscous deformation cycles.

9.2. Origin of Pseudotachylytes at Lower Crustal Conditions

Generation of pseudotachylytes at depths below the classic (10–15 km depth) brittle-ductile transition in the continental crust has been interpreted to result from different processes: (1) frictional melting during

seismic slip, either due to the downward propagation of seismic ruptures nucleated in the upper brittle crust (e.g., Ellis & Stöckhert, 2004; Lin et al., 2005; Moecher & Steltenpohl, 2011) or to the nucleation of lower crustal earthquakes (Austrheim, 2013; Austrheim et al., 2017; Jackson et al., 2004), (2) plastic instabilities (Hobbs et al., 1986; White, 1996, 2012), (3) self-localizing thermal runaway (e.g., Andersen et al., 2014; John et al., 2009), (4) in situ amorphization during high stress deformation at slow displacement rates (Pec et al., 2012). Plastic instabilities and self-localizing thermal runaway require a ductile precursor of a pseudotachylyte-bearing fault. In these models, seismic slip localization and melting result from the feedback between shear heating and thermal softening within a ductile shear zone. However, pseudotachylytes by themselves cannot be taken as unequivocal field evidence for thermal runaway processes, unless they contain clasts of mylonites that could suggest the presence of a ductile precursor. The plastic instability and thermal runaway models do not seem appropriate for the Nusfjord case, because a large amount of pseudotachylytes clearly predates the mylonitic deformation (e.g., Figures 2f and 3f). The pristine pseudotachylytes contain in most of the cases abundant survivor clasts and lithic clasts of the host shattered anorthosite, but not of mylonites (Figure 4a). In situ amorphization is difficult to reconcile with the extensive occurrence of microlites (Figures 4b and 4c), with the formation of chilled margins (Figures 2g and 4d) and with the large volumes of pseudotachylytes. Thus, we interpret the Nusfjord pseudotachylytes as the result of frictional melting on fault planes during seismic slip in the lower crust.

Generation of pseudotachylytes by brittle deformation at lower crustal conditions has been explained by local high fluid pressure promoting fracturing (e.g., Lund & Austrheim, 2003; Steltenpohl et al., 2006). However, the Nusfjord pseudotachylytes are not spatially associated with any vein system, and there is no clear evidence of hydration of the pseudotachylytes with respect to their host rock (Table 1). This is consistent with the development of the Nusfjord pseudotachylytes as the product of coseismic brittle deformation of effectively dry rocks devoid of an intergranular pore fluid. The absence of free aqueous fluid in interconnected intergranular pore space inhibits viscous deformation and results in a high strength of lower crustal rocks (Fitz Gerald et al., 2006). In the absence of elevated pore fluid pressure, high differential stresses are necessary to fracture dry lower crustal rocks. Thus, we interpret the widespread occurrence of pseudotachylytes generated by coseismic brittle deformation in Nusfjord as the evidence of a strong, seismogenic lower crust with a rheology equivalent to that of anhydrous granulite facies material (Jackson et al., 2004; Maggi et al., 2000). Crustal strength calculations suggest that deep seismicity at depths greater than 30 km in the Rukwa-Malawi rift zone is best explained by the rheology of a mafic granulitic lower crust (Fagereng, 2013). Likewise, an analysis of the aftershocks following the 2001 M_w 7.6 Bhuj earthquake revealed that they were indeed located mostly in the lower crust at a depth of about 26 km, and this was explained invoking a mafic granulite rheology of the deeper crustal levels (Bodin & Horton, 2004). Thus, we conclude that the lower crustal Nusfjord earthquakes are consistent with the nucleation of seismic ruptures at depth > 25 km, or with a downward propagation of seismic ruptures from the deep brittle-ductile transition in dry anorthosites, and not from the typical shallower transition in the upper continental crust.

9.3. Deformation Mechanisms in the Mylonitized Pseudotachylytes and the Role of Fluids

Monomineralic plagioclase layers embedded in mylonitized pseudotachylytes show a moderate CPO consistent with dislocation creep by (001) $\frac{1}{2}$ [110] slip system (Figure 7c) (e.g., Kruse et al., 2001). Deformation by dislocation creep in plagioclase monomineralic layers is suggested by the overlap in crystallographic orientation between porphyroclasts and recrystallized grains (Figure 7c), by the excess of low angle boundaries ($<20°$, Figure 7d), and by the clusters of misorientation axes parallel to crystallographic axes for low misorientations ($3-10°$, Figure 7d). Many recrystallized grains show a significant dispersion of crystallographic orientations from the one of the host porphyroclasts (Figure 7c). This is consistent with a contribution of grain boundary sliding after the recrystallization of plagioclase. However, monomineralic layers are typically wrapped by recrystallized pseudotachylytes, and this suggests that the polyphase mixture deriving from recrystallization of pseudotachylytes is rheologically weaker than monomineralic plagioclase domains deforming by dislocation creep.

The fine-grain size of the phase mixture (5–30 μm) and the high degree of phase mixing suggest that mylonitized pseudotachylyte deformed by diffusion creep and grain boundary sliding. The plagioclase weak CPO is not consistent with dislocation creep along common slip systems (Figure 6b). Amphibole has a clear CPO of the (100) planes and [001] direction, but the same CPO has been observed in amphibolites

deformed experimentally in the diffusion creep regime (Getsinger & Hirth, 2014). We interpret the amphibole CPO as the result of oriented grain growth and rigid body rotation during diffusion creep, as concluded for other natural samples deformed at lower crustal condition (e.g., Berger & Stünitz, 1996; Getsinger et al., 2013; Menegon et al., 2015; Okudaira et al., 2015). Thus, we conclude that the brittle grain-size reduction due to pseudotachylyte formation, the fine-grain size, and the polymineralic composition (inhibiting grain growth) of pristine and recrystallized pseudotachylytes (Figures 4c and 4e) predisposed pseudotachylytes veins and the surrounding damage zone to subsequent strain localization by grain size sensitive creep. A similar origin of ultramylonites deforming by grain size sensitive creep was proposed by White (1996), who identified the recrystallization of precursor pseudotachylyte veins as the key grain-size reduction mechanism necessary to produce ultramylonites.

Strain localization triggered by lower crustal seismicity has typically been associated with fluid infiltration and associated reaction weakening in the fractured and hydrated domains (Austrheim, 2013, and references therein). Our results indicate that the formation of mylonitized pseudotachylytes required a six to tenfold increase in H_2O content with respect to the anorthosite protolith (Figures 8b and 9).

In the mylonitized pseudotachylytes, amphibole crystallization in equilibrium with biotite, plagioclase, clinopyroxene, quartz, ilmenite, $\pm$ garnet occurred for H_2O contents above 0.25 wt. % at P = 0.7 GPa and T up to 750°C. At H_2O-undersaturated conditions, amphibole content is strongly dependent on the water content of the system. It is worth noting that at T = 700°C, 0.45 wt. % of water enabling the crystallization of 8 vol. % of amphibole (which represents the average amount of amphibole in the mylonitized pseudotachylytes as estimated with image analysis) is coincident with the limit of H_2O saturation. At higher temperatures, the limit is reached at even lower water contents. This means that very low H_2O is needed to stabilize the observed syndeformation paragenesis and, more important, that 0.25–0.45 wt. % of H_2O is sufficient to saturate the entire rock system at the P, T conditions of deformation. Thus, although H_2O infiltration is required to stabilize the mineral assemblage in the mylonitized pseudotachylytes, the amount of H_2O infiltration that resulted in rheological weakening is minimal. Okudaira et al. (2015) reported similar low values of water contents during diffusion creep deformation in gabbro ultramylonites following a precursor fracturing stage at granulite facies conditions.

This is consistent with experimental results of Milke et al. (2012), which showed that very little amounts of water present as a pore fluid are effective in facilitating mineral reactions if rock deformation maintains a sufficient porosity. Moreover, relatively low water contents ($\sim$0.07 wt. %) are commonly referred to as wet conditions during experimental rock deformation of feldspar rocks in the viscous regime, and are sufficient to activate diffusion creep (Dimanov & Dresen 2005; Rybacki & Dresen, 2000). We argue that brittle grain-size reduction followed by diffusion-accommodated viscous grain boundary sliding enhanced the porosity of the mylonitized pseudotachylytes, and resulted in the distribution of the infiltrated fluids along the grain boundaries. Diffusion-accommodated viscous grain boundary sliding can maintain a dynamic porosity in ultramylonites (Fusseis et al., 2009), which can evolve into the development of creep cavitation bands decorated by new grains that precipitate from the grain boundary fluid (Menegon et al., 2015). In the Nusfjord mylonitized pseudotachylytes, the possible signature of creep cavitation bands is the preferred orientation of amphibole long axis parallel to a C′-type shear band orientation (Figure 6d), similar to the microstructures described in Menegon et al. (2015). The water redistributed along the grain boundaries made the system wet at the shear zone scale, and facilitated heterogeneous phase nucleation, as demonstrated by the synkinematic growth of amphiboles at triple junctions and dilatant sites (Figures 5b and 6a). This stabilized strain localization in the polymineralic, fine-grained mylonitized pseudotachylytes. Therefore, it is the water at grain boundaries that has a major rheological effect on lower crustal shear zones, by facilitating diffusion creep deformation and phase nucleation.

Measurements of intracrystalline water content of plagioclase do not show a systematic increase from the host rock to the pseudotachylytes. This lends further support to our interpretation that the infiltrated aqueous fluid was redistributed along the grain boundaries rather than penetrating the interior of nominally anhydrous minerals via (micro)cracking. The low intracrystalline water contents in plagioclase (Figure 10) were apparently sufficient for limited dislocation creep to occur (Figure 7). However, this did not result in the nucleation of ductile shear zones in intact anorthosites, which instead required a precursor stage of coseismic brittle deformation with associated fluid redistribution at the grain boundaries.
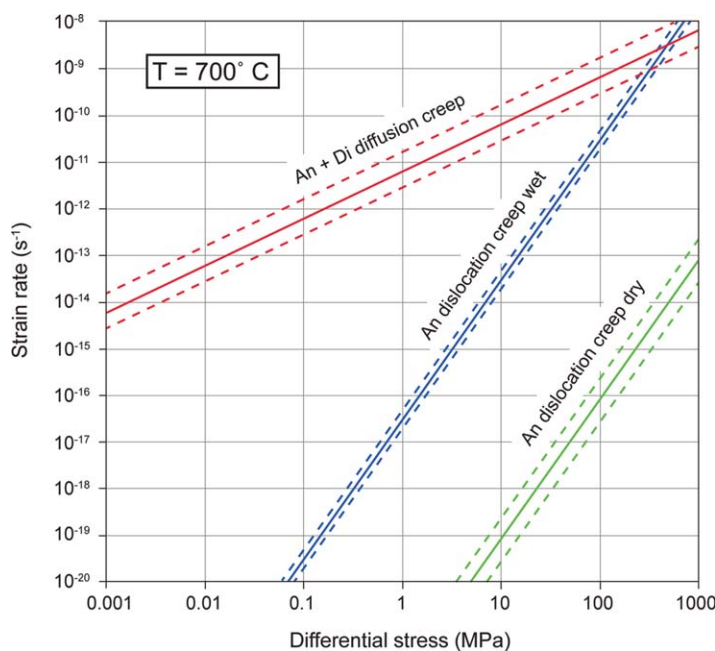
Figure 11. Plot of strain rate (s^{-1}) versus differential stress (MPa) to model the rheology of the mylonitized pseudotachylytes at a temperature of 700°C. The following flow laws were used: anorthite + diopside wet diffusion creep (the An25Di35W flow law of Dimanov & Dresen, 2005), anorthite wet dislocation creep (Rybacki & Dresen, 2000; water content = 0.07 wt. %), anorthite dry dislocation creep (Rybacki & Dresen, 2000; water content = 0.004 wt. %). Dashed lines represent uncertainties in the pre-exponential term A and in the activation energy Q of each flow law. We used the average stress exponents derived experimentally (n = 1 for the diffusion creep flow law, n = 3 for the dislocation creep flow laws).

9.4. Rheology of Mylonitized Pseudotachylytes

To evaluate the extent of weakening resulting from diffusion creep in the mylonitized pseudotachylytes, we compared the rheology of plagioclase deforming by dislocation creep with the rheology of a plagioclase + clinopyroxene aggregate deforming by diffusion creep. The general flow law for dislocation creep is:

$$\dot{\varepsilon} = A\sigma^n \exp\left(-Q/RT\right) \tag{1}$$

where $\dot{\varepsilon}$ is the strain rate, A an empirical constant, σ the differential stress, n the stress exponent, Q the activation energy, R the gas constant, and T the temperature. We used the flow laws for dislocation creep of wet and dry anorthite of Rybacki and Dresen (2000). Dry conditions were chosen to predict the rheology of the anorthosite host rock deforming by dislocation creep and devoid of an intergranular pore fluid phase, whereas wet conditions were chosen to simulate the rheology of monomineralic plagioclase layers embedded in mylonitized pseudotachylytes, which deformed in the presence of H_2O (Figures 4b, and 8).

Deformation accommodated by diffusion creep is described by the flow law:

$$\dot{\varepsilon} = A\sigma^n d^m \exp\left(-Q/RT\right) \tag{2}$$

where d is the grain size and m the grain-size exponent. We used the flow law for diffusion creep of anorthite + diopside aggregates of Dimanov and Dresen (2005). This flow law was chosen because (1) it approximates the composition of the mylonitized pseudotachylytes, and (2) it was derived for grain boundary diffusion-controlled creep, which is consistent with the deformation mechanisms identified in the mylonitized pseudotachylytes. We considered the flow law for wet diffusion creep of an aggregate consisting of 75% anorthite (average grain size of ca. 3.5 μm) and 25% diopside (grain size < 35 μm) (Dimanov & Dresen, 2005).

Rheological calculations show that at T = 700°C the differential stress required to sustain geologically realistic strain rates of 10^{-10}–10^{-13} s^{-1} in the anorthite + diopside aggregate deforming by diffusion creep would be 1–3 orders of magnitude smaller than the stress required to deform plagioclase by wet dislocation creep, and up to 5 orders of magnitude smaller than then stress required to deform plagioclase by dry dislocation creep (Figure 11). Furthermore, in the differential stress range between 10 and 0.1 MPa, deformation by diffusion creep in the anorthite—diopside aggregate would occur 3–7 orders of magnitude faster than deformation by dislocation creep in wet plagioclase. Thus, the weakening from activation of diffusion creep in the fine-grained polyphase mixture derived from recrystallization of pseudotachylytes is predicted to be significant. Similar effects of grain-size reduction, marked weakening, and enhanced creep rates through activation of diffusion creep in recrystallized pseudotachylytes have been proposed by White (1996).

10. Conclusions

In the dry anorthosites from Nusfjord (Lofoten, northern Norway), different generations of pseudotachylytes and mylonites formed at lower crustal conditions of 650–750°C and 0.7–0.9 GPa, as estimated with conventional geothermobarometry and with thermodynamic forward modeling. Mylonites exploited pristine pseudotachylytes veins, which provided both a structural and a compositional precursor for the nucleation of ductile shear zones.

Pristine and mylonitized pseudotachylytes show mutual overprinting relationships that are interpreted as the result of the cyclic interplay between brittle and viscous deformation at lower crustal condition. Pseudotachylytes formed by brittle coseismic deformation in relatively dry and strong anorthosites, as the result of

seismic ruptures nucleated in the deep crust or of the downward propagation of seismic ruptures from the deep brittle-ductile transition in dry anorthosites.

Strain localization in mylonitized pseudotachylytes was facilitated by the grain-size reduction due to the formation and subsequent recrystallization of pseudotachylytes to a fine-grained (< 30 μm) polyphase aggregate. Microstructural observations and EBSD analysis are consistent with diffusion creep as the dominant deformation mechanism in the mylonitized pseudotachylytes. Thermodynamic modeling combined with microstructural observations indicate that the fluid infiltration necessary to stabilize the mineral assemblage of the mylonitized pseudotachylytes was minimal, on the order of 0.20–0.40 wt. % H_2O. The infiltrated aqueous fluid was redistributed along the grain boundaries in the fractured domains, and made the system wet and weak at the shear zone scale. Diffusion-accommodated viscous grain boundary sliding maintained a dynamic porosity in the mylonitized pseudotachylytes, and produced creep cavitation and precipitation of material from grain boundary fluids collected in creep cavities and in other dilatant sites.

Extrapolation of experimentally derived flow laws to geologically realistic strain rates at a temperature of 700°C indicates up to 3 orders of magnitude weakening in the mylonitized pseudotachylytes deforming by diffusion creep with respect to plagioclase deforming by dislocation creep in the anorthosite host rock. This highlights that pseudotachylytes caused by brittle faulting can be precursors of viscous, weak shear zones in the dry lower crust, indicating lower crustal earthquakes as agents of rheological change from strong, brittle crust, to strong crust with embedded fine-grained, weak viscous shear zones.

References

Andersen, T. B., Austrheim, H., Deseta, N., Silkoset, P., & Ashwal, L. D. (2014). Large subduction earthquakes along the fossil Moho in Alpine Corsica. *Geology*, *42*, 395–398. https://doi.org/10.1130/G35345.1

Anderson, J. L., & Smith, D. R. (1995). The effects of temperature and fO_2 on the Al-in-hornblende barometer. *American Mineralogist*, *80*, 549–559.

Austrheim, H. (2013). Fluid and deformation induced metamorphic processes around Moho beneath continent collision zones: Examples from the exposed root zone of the Caledonian mountain belt, W-Norway. *Tectonophysics*, *609*, 620–635.

Austrheim, H., & Blundy, T. M. (1994). Pseudotachylytes generated during seismic faulting and eclogitization of the deep crust. *Science*, *265*, 82–83.

Austrheim, H., Dunkel, K. G., Plümper, O., Ildefonse, B., Liu, Y., & Jamtveit, B. (2017). Fragmentation of wall rock garnets during deep crustal earthquakes. *Science Advances*, *3*, e1602067.

Berger, A., & Stünitz, H. (1996). Deformation mechanisms and reaction of hornblende: Examples from the Bergell Tonalite (Central Alps). *Tectonophysics*, *257*, 149–174.

Bodin, P., & Horton, S. (2004). Source parameters and tectonic implications of aftershocks of the Mw 7.6 Bhuj earthquake of 26 January 2001. *Bulletin of the Seismological Society of America*, *94*, 818–827.

Chen, W.-P., & Molnar, P. (1983). Focal depths of intracontinental and intraplate earthquakes and their implications for the thermal and mechanical properties of the lithosphere. *Journal of Geophysical Research*, *88*, 4183–4214.

Connolly, J. A. D. (2005). Multivariable phase diagrams: An algorithm based on generalized thermodynamics. *American Journal of Science*, *290*, 666–718.

Corfu, F. (2004). U–Pb Age, setting and tectonic significance of the Anorthosite–Mangerite–Charnockite–Granite Suite, Lofoten–Vesterålen, Norway. *Journal of Petrology*, *45*, 1799–1819.

Dale, J., Powell, R., White, R. W., Elmer, F. L., & Holland, T. J. B. (2005). A thermodynamic model for Ca-Na clinoamphiboles in Na2O-CaO-FeO-MgO-Al2O3-SiO2-H2O-O for petrological calculations. *Journal of Metamorphic Geology*, *23*, 771–791.

Dimanov, A., & Dresen, G. (2005). Rheology of synthetic anorthite-diopside aggregates: Implications for ductile shear zones. *Journal of Geophysical Research*, *110*, B07203. https://doi.org/10.1029/2004JB003431

Di Toro, G., & Pennacchioni, G. (2005). Fault plane processes and mesoscopic structure of a strong-type seismogenic fault in tonalites (Adamello batholith, Southern Alps. *Tectonophysics*, *402*, 55–80. https://doi.org/10.1016/j.tecto.2004.12.036

Ellis, S., & Stöckhert, B. (2004). 0, Elevated stresses and creep rates beneath the brittle-ductile transition caused by seismic faulting in the upper crust. *Journal of Geophysical Research*, *109*, B05407. https://doi.org/10.1029/2003JB002744

Fagereng, Å. (2013). Fault segmentation, deep rift earthquakes and crustal rheology: Insights from the 2009 Karonga sequence and seismicity in the Rukwa–Malawi rift zone. *Tectonophysics*, *601*, 216–225.

Fitz Gerald, J. D., N. S., Mancktelow, G., Pennacchioni, K., & Kunze, K. (2006). Ultrafine-grained quartz mylonites from high-grade shear zones: Evidence for strong and dry middle to lower crust. *Geology*, *34*, 369–372.

Fusseis, F., Regenaure-Lieb, K., Liu, J., Hough, R. M., & De Carlo, F. (2009). Creep cavitation can establish a dynamic granular fluid pump in ductile shear zones. *Nature*, *459*, 974–977. https://doi.org/10.1038/nature08051

Getsinger, A. J., & Hirth, G. (2014). Amphibole fabric formation during diffusion creep and the rheology of shear zones. *Geology*, *42*, 535–538.

Getsinger, A. J., Hirth, G., Stünitz, H., & Goergen, E. T. (2013). Influence of water on rheology and strain localization in the lower continental crust. *Geochemistry, Geophysics, Geosystems*, *14*, 2247–2264. https://doi.org/10.1002/ggge.20148

Griffin, W. L., Taylor, P. N., Hakkinen, J. W., Heier, K. S., Iden, I. K., Krogh, E. J., . . . Tveten, E. (1978). Archaean and Proterozoic crustal evolution in Lofoten-Vesterålen, N Norway. *Journal of the Geological Society of London*, *135*, 629–647.

Handy, M. R., & Brun, J.-P. (2004). 0, Seismicity, structure and strength of the continental lithosphere. *Earth and Planetary Science Letters*, *223*, 427–441.

Hobbs, B. E., Ord, A., & Teyssier, C. (1986). Earthquakes in the Ductile Regime? *Pure and Applied Geophysics*, *124*, 309–336.

Holland, T., & Blundy, J. (1994). Non-ideal interactions in calcic amphiboles and their bearing on amphibole-plagioclase thermometry. *Contributions to Mineralogy and Petrology*, *116*, 433–447.

Holland, T. J. B., & Powell, R. (1998). An internally consistent thermodynamic data set for phases of petro- logic interest. *Journal of Metamorphic Geology*, *16*, 309–343.

Holland, T. J. B., & Powell, R. (2003). Activity-composition relations for phases in petrological calculations: An asymmetric multicomponent formulation. *Contributions to Mineralogy and Petrology*, *145*, 492–501.

Jackson, J. A., Austrheim, H., McKenzie, D., & Priestley, K. (2004). Metastability, mechanical strength, and the support of mountain belts. *Geology*, *32*, 625–628.

John, T., Medvedev, S., Ruepke, L. H., Andersen, T. B., Podladchikov, Y. Y., & Austrheim, H. (2009). Generation of intermediate-depth earthquakes by self-localizing thermal runaway. *Nature Geoscience*, *2*, 137–140.

Kruse, R., Stünitz, H., & Kunze, K. (2001). Dynamic recrystallization processes in plagioclase porphyroclasts. *Journal of Structural Geology*, *23*, 1781–1802.

Kullerud, K., Flaat, K., & Davidsen, B. (2001). High-pressure fluid-rock reactions involving cl-bearing fluids in lower-crustal ductile shear zones of the flakstadøy basic complex, Lofoten, Norway. *Journal of Petrology*, *42*, 1349–1372.

Leib, S. E., Moecher, D. P., Steltenpohl, M. G., & Andresen, A. (2016). Thermobarometry of metamorphosed pseudotachylyte and associated mylonite: Constraints on dynamic Co-seismic rupture depth attending Caledonian extension, North Norway. *Tectonophysics*, *682*, 85–95.

Lesne, P., Kohn, S. C., Blundy, J., Witham, F., Botcharnikov, R. E., & Behrens, H. (2011). Experimental simulation of closed-system degassing in the system basalt–H2O–CO2–S–Cl. *Journal of Petrology*, *52*, 1737–1762.

Lin, A., Maruyama, T., Stallard, A., Michibayashi, K., Camacho, A., & Kano, K-I. (2005). Propagation of seismic slip from brittle to ductile crust: Evidence from pseudotachylytes of the Woodroffe thrust, central Australia. *Tectonophysics*, *402*, 21–35.

Lund, M. G., & Austrheim, H. (2003). High-pressure metamorphism and deep-crustal seismicity: Evidence from contemporaneous formation of pseudotachylytes and eclogite facies coronas. *Tectonophysics*, *372*, 59–83. https://doi.org/10.1016/S0040-1951(03)00232-4

Maggi, A., Jackson, J. A., McKenzie, D., & Priestley, K. (2000). Earthquake focal depths, effective elastic thickness, and the strength of the continental lithosphere. *Geology*, *28*, 495–498.

Markl, G., Frost, B. R., & Bucher, K. (1998). The origin of anorthosites and related rocks from the Lofoten Islands, Northern Norway: I. Field relations and estimation of intrinsic variables. *Journal of Petrology*, *39*, 1425–1452.

McKenzie, D., & Brune, J. N. (1972). Melting on fault planes during large earthquakes. *Geophysical Journal of the Royal Astronomical Society*, *29*, 65–78.

Menegon, L., Nasipuri, P., Stünitz, H., Behrens, H., & Ravna, E. (2011). Dry and strong quartz during deformation of the lower crust in the presence of melt. *Journal of Geophysical Research*, *116*, B10410. https://doi.org/10.1029/2011JB008371

Menegon, L., Stünitz, H., Nasipuri, P., Heilbronner, R., & Svahnberg, H. (2013). Transition from fracturing to viscous flow in granulite facies perthitic feldspar (Lofoten, Norway). *Journal of Structural Geology*, *48*, 95–112.

Menegon, L., Fusseis, F., Stünitz, H., & Xiao, X. (2015). Creep cavitation bands control porosity and fluid flow in lower crustal shear zones. *Geology*, *43*, 227–230. https://doi.org/10.1130/G36307.1

Milke, R., Neusser, G., Kolzer, K., & Wunder, B. (2012). Very little water is necessary to make a dry solid silicate system wet. *Geology*, *41*, 247–250.

Moecher, D. P., & Steltenpohl, M. G. (2009). Calculation of rupture depth for an exhumed paleoseismogenic fault from mylonitic pseudotachylyte. *Geology*, *37*, 999–1002.

Moecher, D. P., & Steltenpohl, M. G. (2011). Petrologic evidence for seismogenic slip in extending middle to lower continental crust: Heier's Zone of pseudotachylyte, North Norway, in Geology of the Earthquake Source: A volume in Honour of Rick Sibson. *Geological Society Special Publication*, *359*, 169–186.

Okudaira, T., Jeřábek, P., Stünitz, H., & Fusseis, F. (2015). High-temperature fracturing and subsequent grain-size-sensitive creep in lower crustal gabbros: Evidence for coseismic loading followed by creep during decaying stress in the lower crust? *Journal of Geophysical Research: Solid Earth*, *120*, 3119–3141. https://doi.org/10.1002/2014JB011708

Okudaira, T., Shigematsu, N., Harigane, Y., & Yoshida, K. (2017). Grain size reduction due to fracturing and subsequent grain-size-sensitive creep in a lower crustal shear zone in the presence of a CO2-bearing fluid. *Journal of Structural Geology*, *95*, 171–187.

Pec, M., Stünitz, H., Heilbronner, R., Drury, M., & de Capitani, C. (2012). Origin of pseudotachylytes in slow creep experiments. *Earth and Planetary Science Letters*, *355–356*, 299–310.

Pennacchioni, G. (2005). Control of the geometry of precursor brittle structures on the type of ductile shear zone in the Adamello tonalites, Southern Alps (Italy). *Journal of Structural Geology*, *27*, 627–644. https://doi.org/10.1016/j.jsg.2004.11.008

Pennacchioni, G., & Cesare, B. (1997). Ductile-brittle transition in pre-Alpine amphibolite-facies mylonites during evolution from water-present to water-deficient conditions (Mont Mary nappe, Italian Western Alps). *Journal of Metamorphic Geology*, *15*, 777–791.

Pennacchioni, G., & Mancktelow, N. S. (2007). Nucleation and initial growth of a shear zone network within compositionally and structurally heterogeneous granitoids under amphibolite facies conditions. *Journal of Structural Geology*, *29*, 1757–1780. https://doi.org/10.1016/j.jsg.2007.06.002

Pennacchioni, G., & Zucchi, E. (2013). High-temperature fracturing and ductile deformation during cooling of a pluton: The Lake Edison granodiorite (Sierra Nevada batholith, California). *Journal of Structural Geology*, *50*, 54–81. https://doi.org/10.1016/j.jsg.2012.06.001

Pittarello, L., Pennacchioni, G., & Di Toro, G. (2012). Amphibolite-facies pseudotachylytes in Premosello metagabbros and felsic mylonites (Ivrea Zone, Italy). *Tectonophysics*, *580*, 43–57. https://doi.org/10.1016/j.tecto.2012.08.001

Rybacki, E., & Dresen, G. (2000). Dislocation and diffusion creep of synthetic anorthite aggregates. *Journal of Geophysical Research*, *105*, 16017–26036.

Steltenpohl, M. G., Hames, W. E., & Andresen, A. (2004). The Silurian to Permian history of a metamorphic core complex in Lofoten, northern Scandinavian Caledonides. *Tectonics*, *23*, TC1002.

Steltenpohl, M. G., Kassos, G., & Andresen, A. (2006). Retrograded eclogite-facies pseudotachylites as deepcrustal paleoseismic faults within continental basement of Lofoten, north Norway. *Geosphere*, *2*, 61–72.

Steltenpohl, M. G., Kassos, G., Andresen, A., Rehnström, E. F., & Hames, W. E. (2011). Eclogitization and exhumation of Caledonian continental basement in Lofoten, North Norway. *Geosphere*, *7*, 1–17.

Stünitz, H., Thust, A., Heilbronner, R., Behrens, H., Kilian, R., Tarantola, A., & Fitz Gerald, J. D. (2017). Water redistribution in experimentally deformed natural milky quartz single crystals: Implications for H2O-weakening processes. *Journal of Geophysical Research: Solid Earth*, *122*, 866–894. https://doi.org/10.1002/2016JB013533

Tajcmanova, L., Connolly, J. A. D., & Cesare, B. (2009). A thermodynamic model for titanium and ferric iron solution in biotite. *Journal of Metamorphic Geology*, *27*, 153–165.

White, J. C. (1996). Transient discontinuities revisited: Pseudotachylyte, plastic instability and the influence of low pore fluid pressure on deformation processes in the mid-crust. *Journal of Structural Geology*, *18*, 1471–1486.

White, J. C. (2012). Paradoxical pseudotachylytes: Fault melt outside the seismogenic zone. *Journal of Structural Geology*, *38*, 11–20.

Wright, T. J., Elliott, J. R., Wang, H., & Ryder, I. (2013). Earthquake cycle deformation and the Moho: Implications for the rheology of the continental lithosphere. *Tectonophysics*, *609*, 504–523.